

Electronic Supplementary Information for

NIR-Selective Electrochromic Heteromaterial Frameworks: a Platform to Understand Mesoscale Transport Phenomena in Solid-State Electrochemical Devices

Teresa E. Williams,^{a,b} Christina M. Chang,^{a,†} Evelyn L. Rosen,^a Guillermo Garcia,^c
Evan L. Runnerstrom,^{a,d} Bradley L. Williams,^a Bonil Koo,^c Raffaella Buonsanti,^{e,f}
Delia J. Milliron^{a,g,*} and Brett A. Helms^{a,*}

^a The Molecular Foundry, Lawrence Berkeley National Laboratory, 1 Cyclotron Road, Berkeley, CA 94720 (USA).

^b Graduate Group in Applied Science and Technology, University of California, Berkeley, CA 94720 (USA).

^c Heliotrope Technologies, 2625 Alcatraz Ave #377, Berkeley CA 94705 (USA).

^d Department of Materials Science and Engineering, University of California, Berkeley, CA 94720 (USA).

^e Joint Center for Artificial Photosynthesis, Lawrence Berkeley National Laboratory, 2929 7th Street, Berkeley, CA 94710 (USA).

^f Materials Sciences Division, Lawrence Berkeley National Laboratory, 1 Cyclotron Road, Berkeley, CA 94720 (USA).

^g Department of Chemical Engineering, The University of Texas at Austin, 200 E. Dean Keeton Street, Austin, TX 78712 (USA).

† C.M.C.'s current address: Department of Chemistry, University of Cambridge, Lensfield Road, Cambridge, CB2 1EW (UK)

* Any correspondence should be directed to: milliron@che.utexas.edu, bahelms@lbl.gov

This PDF includes:
Figures S1 to S12
Additional Technical Notes

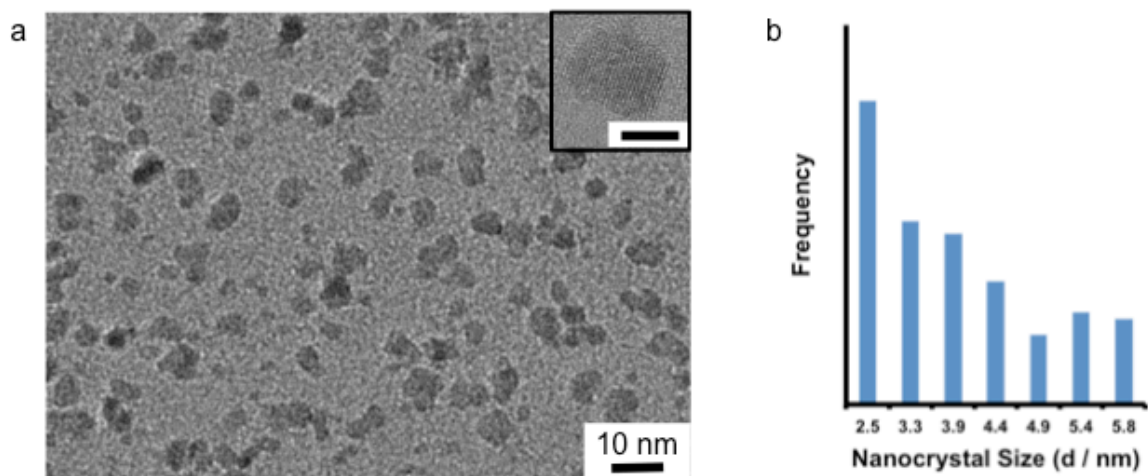


Figure S1. Transmission electron microscopy image (a) and size distribution (b) of ITO nanocrystals. Inset scale bar is 4 nm.

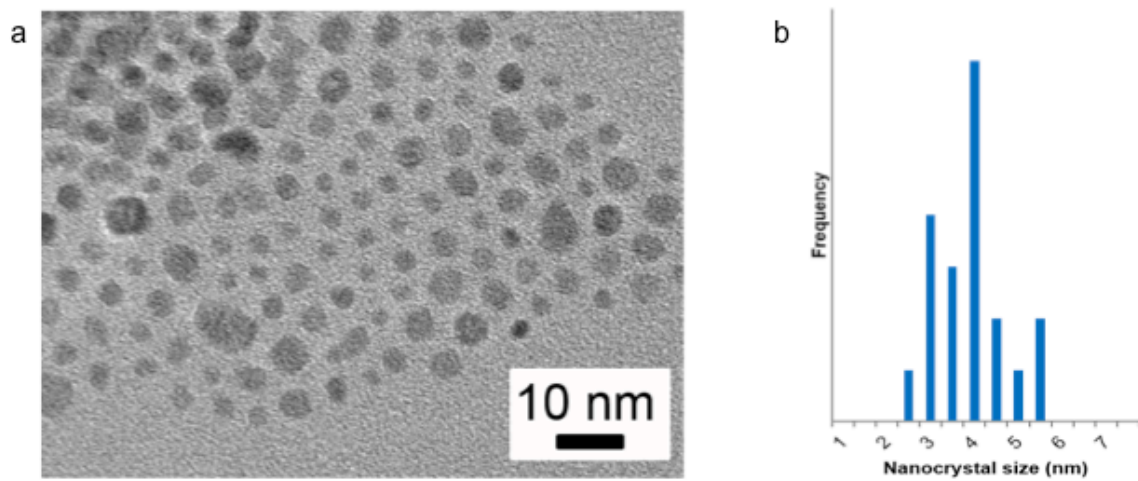


Figure S2. Transmission electron microscopy image (a) and size distribution (b) of CeO₂ nanocrystals.

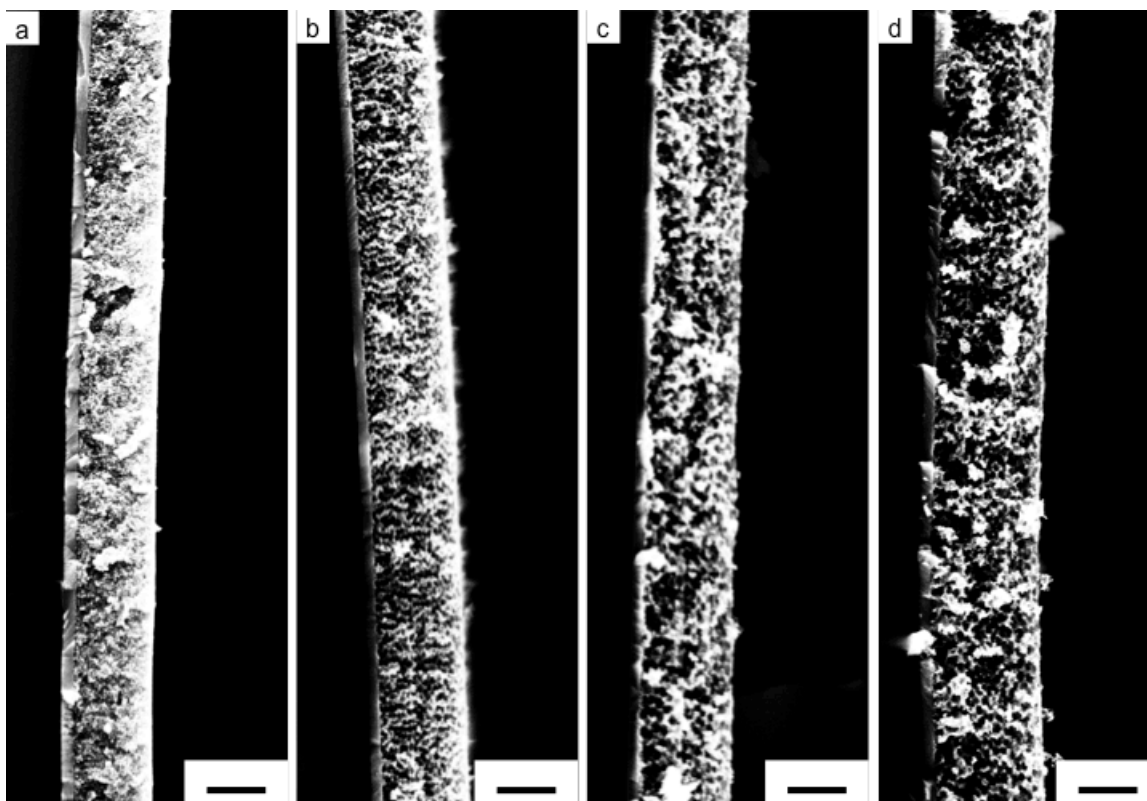


Figure S3. Cross-sectional scanning electron micrographs of ITO nanocrystal films: unarchitected films (a) are shown alongside those assembled into hierarchically porous films using PDMA_{20k}-*b*-PS_{20k} (b), PDMA_{10k}-*b*-PS_{60k} (c), or PDMA_{20k}-*b*-PS_{60k} (d) block copolymer as architecture-directing agents. All scale bars are 200 nm.

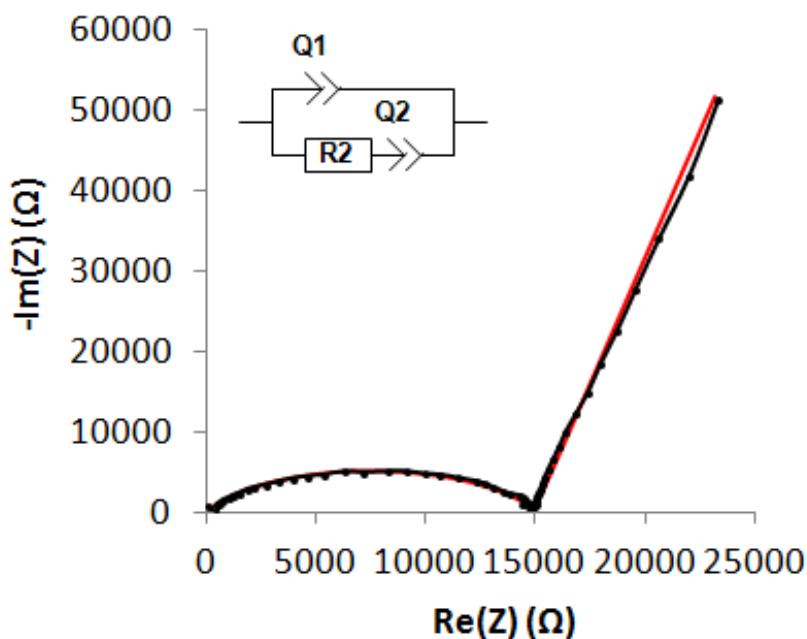


Figure S4. Nyquist plot for the plasticized polymer electrolyte (PPE) (black line and data points) and fit calculated using the equivalent circuit model shown (inset and red line). Q1 and Q2 are constant phase elements, and R2 is a resistor. To provide a direct comparison to the PPE films used for devices, a dried film of PPE was pressed between two ITO-coated substrates which functioned as the working and counter electrodes using a two-electrode configuration. A 50 μm spacer defined the electrolyte thickness. Electrochemical impedance spectroscopy was obtained in the frequency range of 1 MHz to 1 Hz with 10 frequency points per logarithmic decade and an oscillation voltage of 10 mV. The above Nyquist plot was used to determine the room-temperature ionic conductivity for the PPE, $\sigma = 1.1 \times 10^{-7} \text{ S cm}^{-1}$.

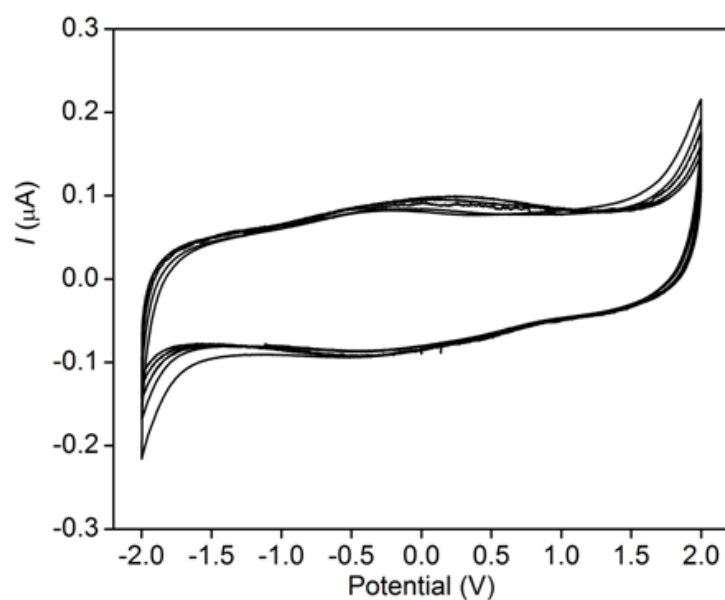


Figure S5. Cyclic voltammetry for the same PPE film as in Figure S4 at 10 mV s^{-1} scan rate in the potential range of -2 to +2 V. The first of 5 cycles has been omitted. The potential stability window for the PPE was taken to be -1.8 to +1.8 V.

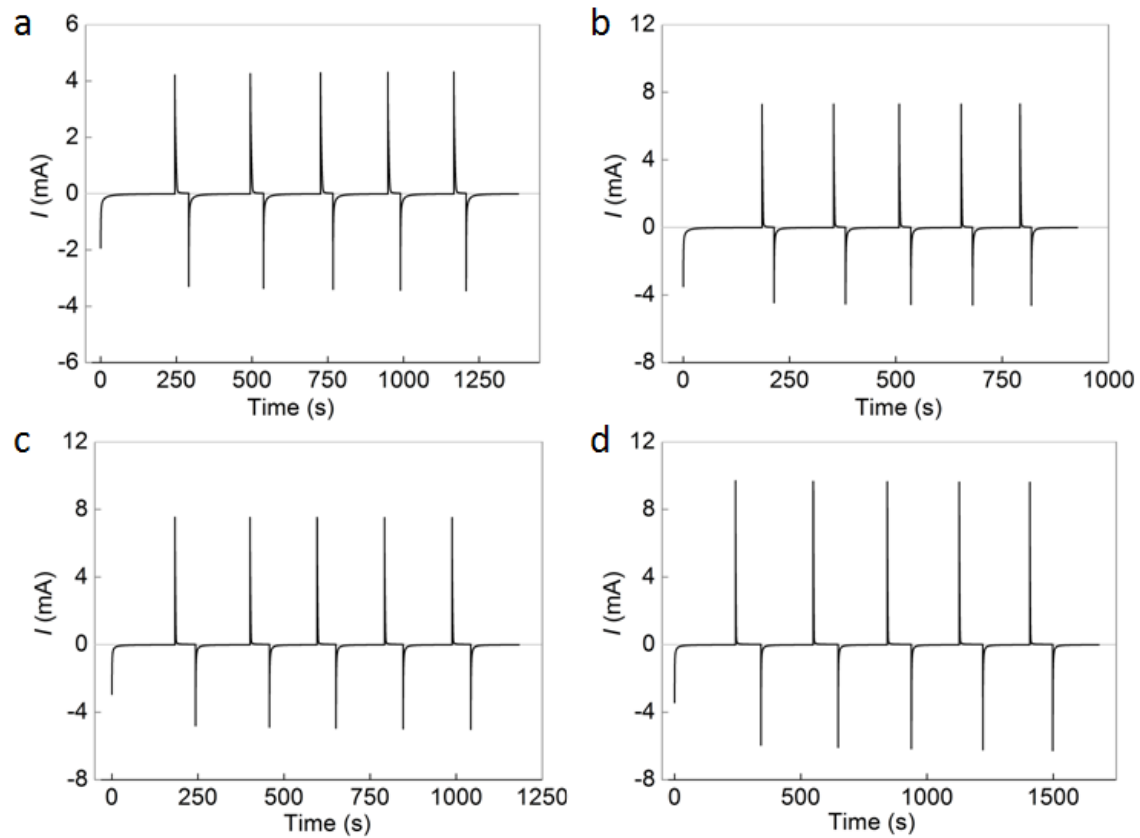


Figure S6. Chronoamperometry data for all ITO nanocrystal films: unarchitected films (a) are shown alongside those assembled into hierarchically porous films using PDMA_{20k}-*b*-PS_{20k} (b), PDMA_{10k}-*b*-PS_{60k} (c), or PDMA_{20k}-*b*-PS_{60k} (d) block copolymers as architecture-directing agents. A voltage swing of 1.8 and 4.0 V vs. Li/Li⁺ was used for all films.

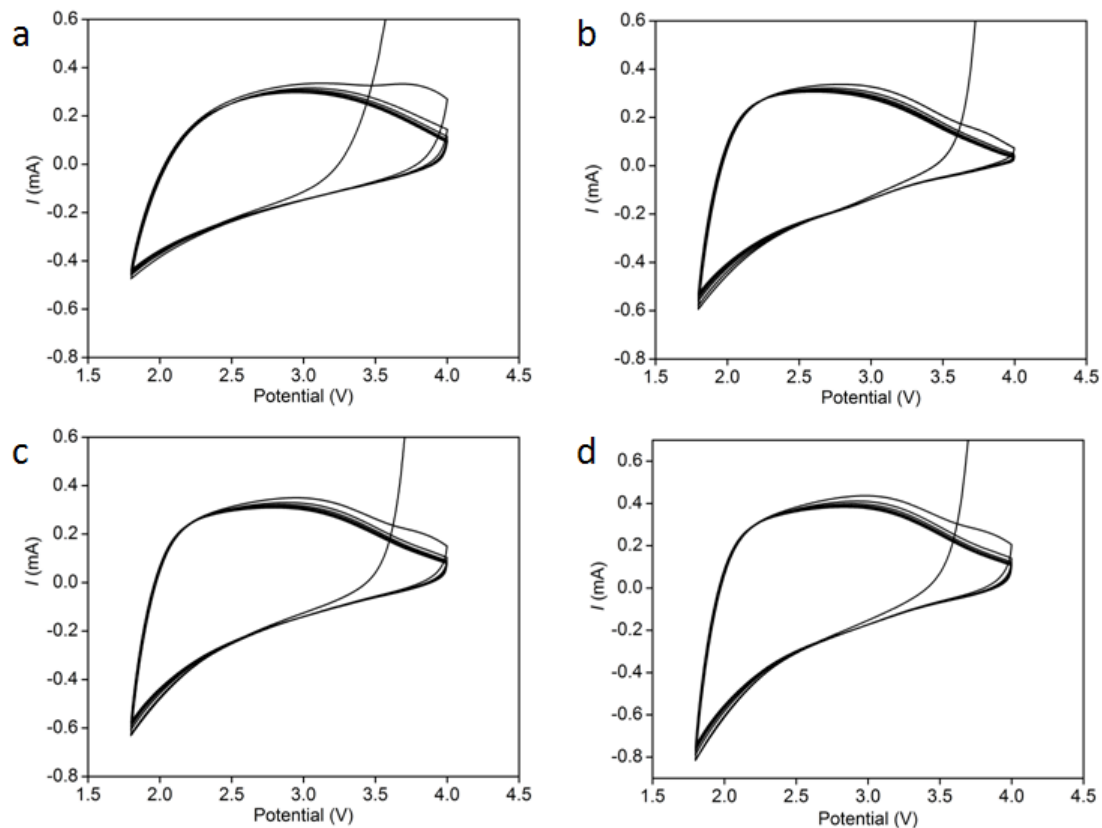


Figure S7. Cyclic voltammetry for ITO films at a 100 mV s^{-1} scan rate over a potential range of 1.8 to 4 V vs. Li/Li^+ . Data are shown for unarchitected films (a) alongside those assembled into hierarchically porous films using $\text{PDMA}_{20\text{k}}\text{-}b\text{-PS}_{20\text{k}}$ (b), $\text{PDMA}_{10\text{k}}\text{-}b\text{-PS}_{60\text{k}}$ (c), or $\text{PDMA}_{20\text{k}}\text{-}b\text{-PS}_{60\text{k}}$ (d) block copolymers as architecture-directing agents. Charging capacity was determined by integration of the charging curve for each cycle after discarding the first and last cycle of the six cycles measured.

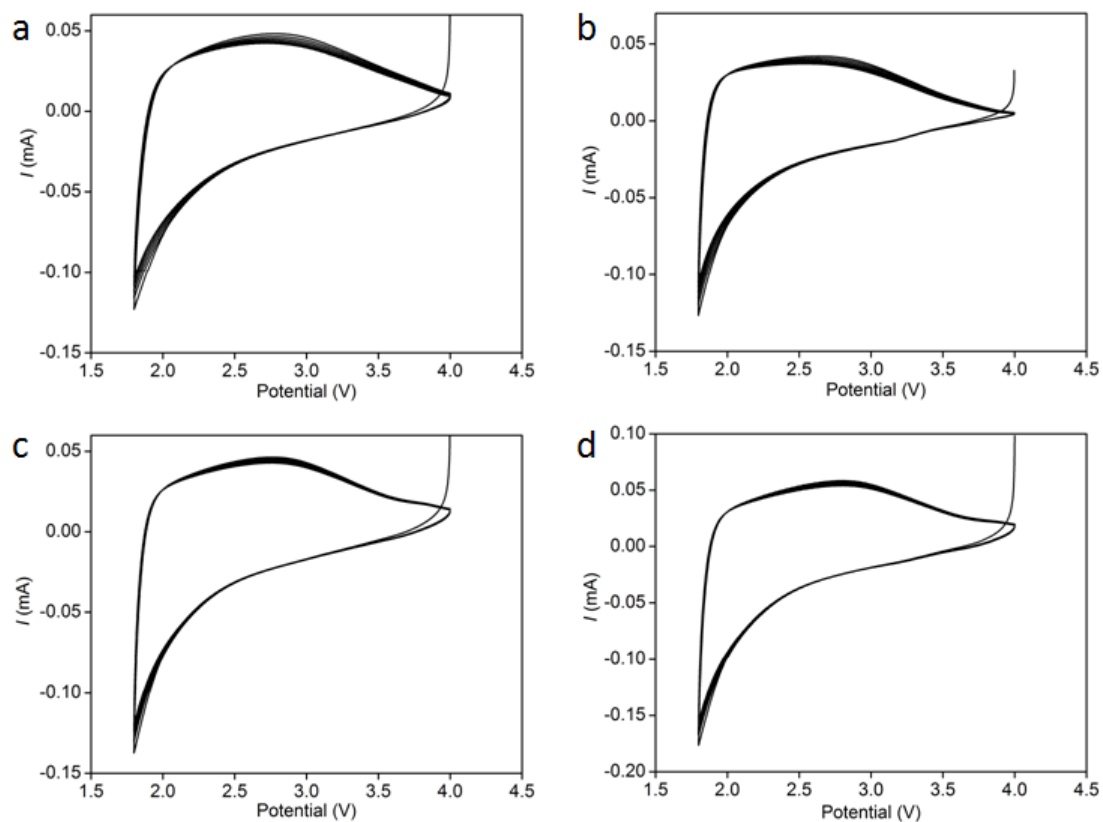


Figure S8. Cyclic voltammetry for ITO films at a 10 mV s^{-1} scan rate over a potential range of 1.8 to 4 V vs. Li/Li⁺. Data are shown for unarchitected films (a) alongside those assembled into hierarchically porous films using PDMA_{20k}-*b*-PS_{20k} (b), PDMA_{10k}-*b*-PS_{60k} (c), or PDMA_{20k}-*b*-PS_{60k} (d) block copolymers as architecture-directing agents. Charging capacity was determined by integration of the charging curve for each cycle after discarding the first and last cycle of the six cycles measured.

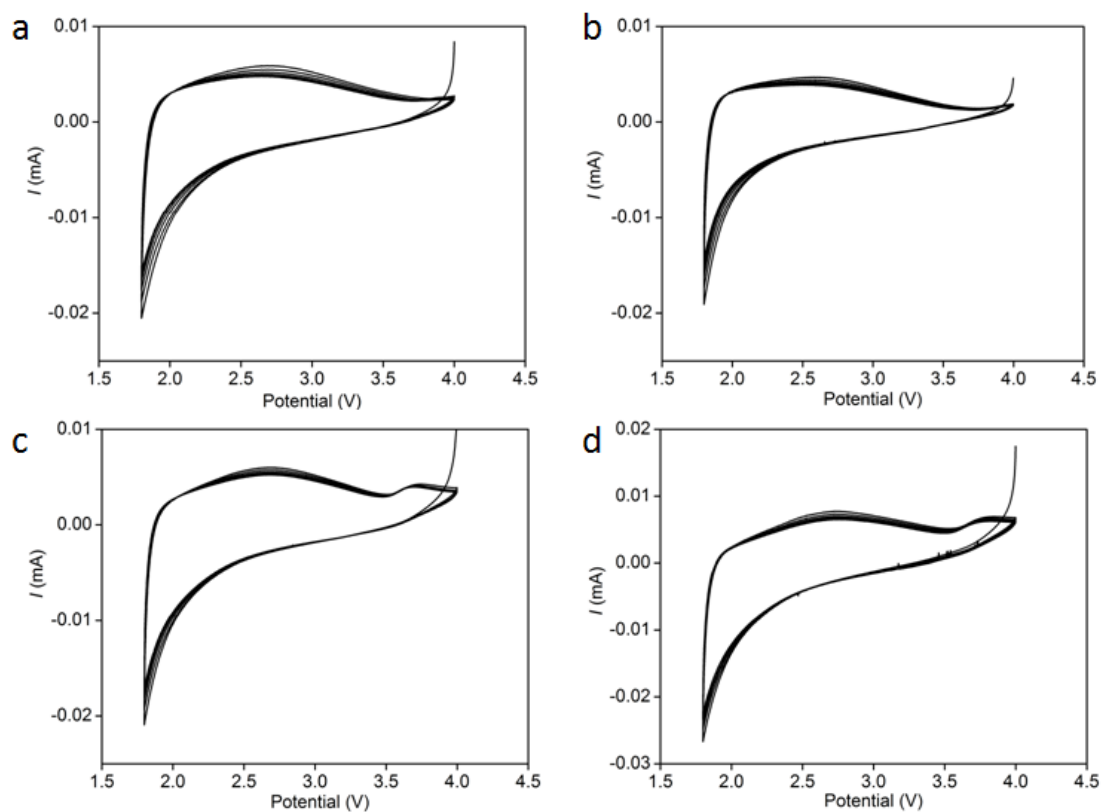


Figure S9. Cyclic voltammetry for ITO films at a 1 mV s^{-1} scan rate over a potential range of 1.8 to 4 V vs. Li/Li^+ . Data are shown for unarchitected films (a) alongside those assembled into hierarchically porous films using PDMA_{20k}-*b*-PS_{20k} (b), PDMA_{10k}-*b*-PS_{60k} (c), or PDMA_{20k}-*b*-PS_{60k} (d) block copolymers as architecture-directing agents. Charging capacity was determined by integration of the charging curve for each cycle after discarding the first and last cycle of the six cycles measured.

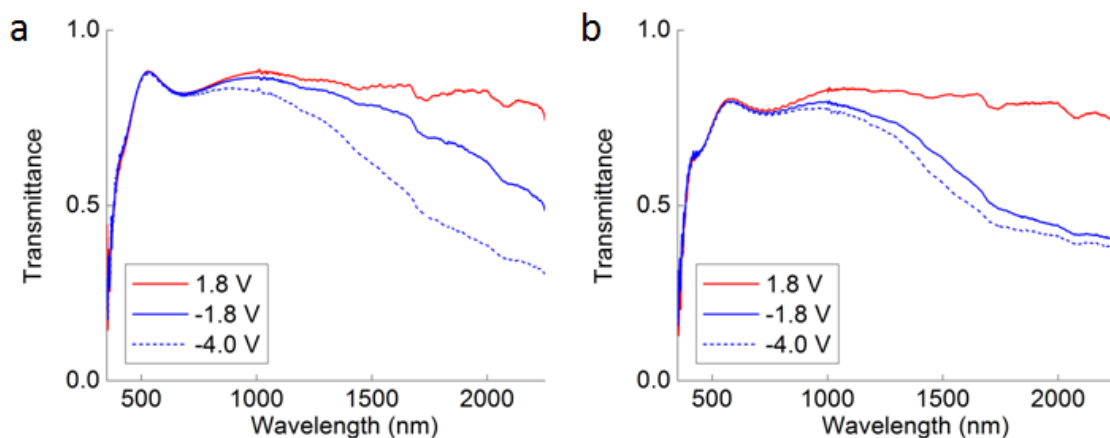


Figure S10. Optical modulation in solid-state NIR-electrochromic devices: ~258 nm unarchitected ITO active layers (a) are shown alongside ~309 nm hierarchically porous ITO active layers (b) generated using PDMA_{20k}-b-PS_{20k} architecture-directing agents. An initial break-in step was carried out by applying a -4 V bias across the device; ITO charging at that potential after 6 min signifies the maximum extent of NIR-blocking available to the device (dotted blue). Under normal operation, SS devices were switched between -1.8 V and +1.8 V to achieve NIR-blocking (solid blue) and NIR-transmissive (solid red) states, respectively. The absolute transmittance traces shown here were normalized to the trace at +1.8 V (i.e., SS_{off} in Figure 7 in the main text) to show ΔT in the NIR-transmissive and NIR-blocking states in Figure 7.

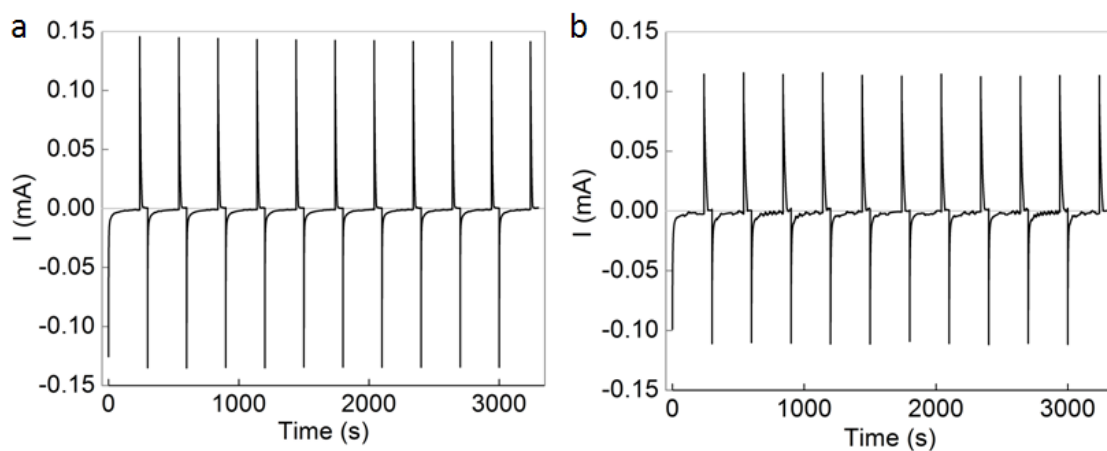


Figure S11. Chronoamperometry data for solid-state devices configured with NIR-switchable ITO nanocrystal electrodes. Data are shown for an unarchitected ITO NC film (a) as well as a hierarchically porous film using PDMA_{20k}-b-PS_{20k} block copolymer as an architecture-directing agent. (b). A two-electrode configuration was used with -1.8 and +1.8 voltage swings for 4 min and 1 min, respectively.

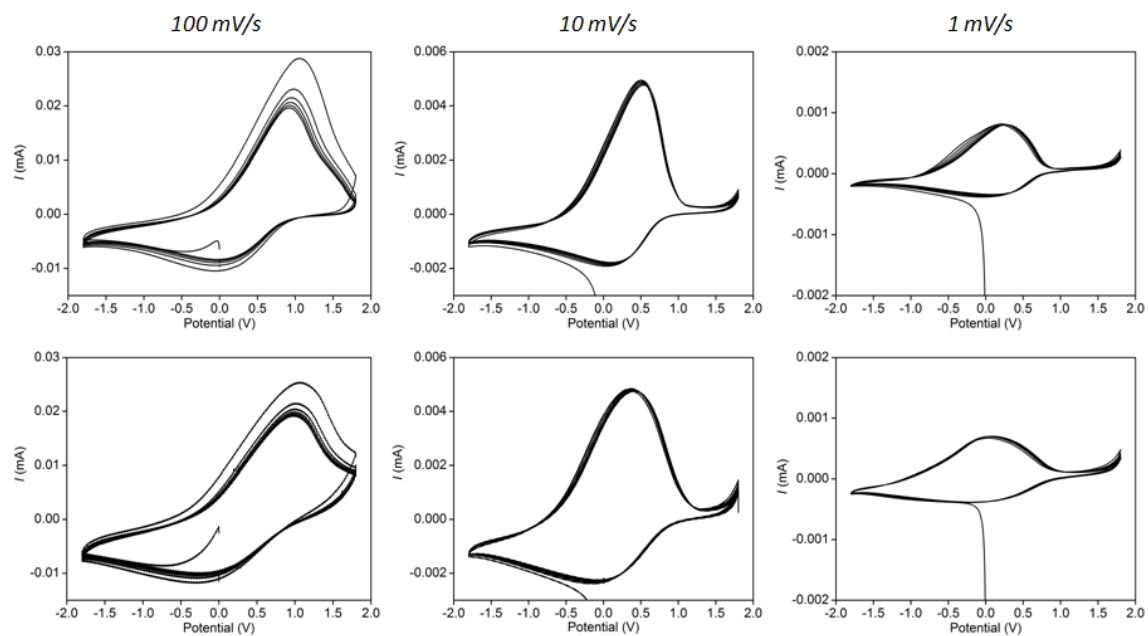


Figure S12. Cyclic voltammetry for solid-state devices at different scan rates. The top row shows cyclic voltammograms (CVs) for an unarchitected ITO device, while the bottom row shows CVs for a PDMA_{20k}-*b*-PS_{20k}-architected device obtained at three scan rates: 100 mV s⁻¹ (left column), 10 mV s⁻¹ (middle column), and 1 mV s⁻¹ (right column). Charging capacity was determined by integration of the charging curve for each cycle after discarding the first and last of six cycles measured.

Additional Technical Notes:

(1) Units of F (Farads) – defined as the charge in Coulombs that a capacitor will accept for the potential across it to change by 1 V – are common when reporting data for the charging (and discharging) of electrochemical capacitors. For our work, however, we were interested in determining the *specific capacity* of our electrodes, which we reported in units of C/g. We calculated specific capacity by integrating the *i-V* curves as described in the main text over the potential range of the measurement (representing the total amount of stored charge), then normalizing to the mass of ITO on the electrode. As our measurements had a voltage sweep greater than 1 V, this value was never referred to as a *capacitance*. Our use of *specific capacity* was useful in quantifying differences in the optical performance of the different architected mesoporous ITO NC electrodes and polymer electrolyte-infiltrated heteromaterial frameworks over the wide voltage range needed for device switching, as described in detail in the main text.

(2) Unarchitected NC-only films have more surface area (theoretically) than any of the architected films, since there are more ITO nanocrystals per unit volume. Nevertheless, each of the architected films showed greater specific capacity than the unarchitected ITO NC films. Based on our data, we reasoned that this increase is due to improvements in how the mesoporous films charge (and discharge) the electrical double layer (EDL) during switching. In the unarchitected NC-only films, there are only micropores (0.5-2 nm) and thus significant overlap in the EDLs, which has been reported to limit ion transport and overall charge capacity (see for example, *JACS* **2008**, *130*, 2730; *JACS* **2009**, *131*, 1802). We hypothesize that all of our architecture-directing agents regularly spaces the ITO in space so as to minimize charging inefficiencies related to overlapping double layers. It may yet be possible to reduce the dimensions of the mesopores so that critical behavior is revealed deliberately (e.g., mesopores spanning a range of 2-10 nm). For the present work, however, the larger end of the mesopore sizes was used and thought to aid in back-filling with the plasticized polymer electrolyte (PPE).

(3) The extent of PPE oxidation was monitored during the break-in step using spectroelectrochemistry. When a potential bias of -4 V is applied across the device, oxidation of the PPE with coupled charge injection into the ITO layer leads to plasmon absorption, observed as NIR blocking in the optical spectrum. Qualitatively, the plasmon absorption can be monitored until no further change in the optical spectrum occurs, at which point sufficient PPE oxidation has occurred. This state of the device is summarized in Figure 7.

(4) Long-term cycling or photostability of these devices is not yet known; nonetheless, our materials were selected with long device lifetimes in mind. Polyvinyl butyral has been used extensively in the glass lamination industry due to its high photo- and thermal stability. Our manuscript presents data and conclusions inferred from at least 10 cycles for these devices, which was sufficient to observe differences in the utilization of active material.